ADVANCED MATERIALS

Supporting Information

for *Adv. Mater.*, DOI: 10.1002/adma.201700212

Anomalous Resistance Hysteresis in Oxide ReRAM: Oxygen Evolution and Reincorporation Revealed by In Situ TEM

David Cooper, Christoph Baeumer,* Nicolas Bernier, Astrid Marchewka, Camilla La Torre, Rafal E. Dunin-Borkowski, Stephan Menzel, Rainer Waser, and Regina Dittmann*

SUPPORTING INFORMATION

SAMPLE FABRICATION AND *IN-SITU* CONTACTING

A 20 nm single-crystalline undoped $SrTiO_3$ thin film with a 2-3% Sr excess was fabricated using pulsed laser deposition on a 0.5-wt% Nb:$SrTiO_3$ substrate (CrysTec GmbH, Germany). The single-crystalline $SrTiO_3$ target was ablated by a KrF excimer laser (λ = 248 nm) with a repetition rate of 5 Hz and a spot size of 2 mm^2 at a target-to-substrate distance of 44 mm. The laser fluence was 1.05 J cm^{-2}. The sample was grown in an oxygen atmosphere of 0.1 mbar at a substrate temperature of 800 °C. Film growth was monitored using reflection high-energy electron diffraction.

A top electrode was formed using electron beam evaporation of 10 nm of Pt and patterning through optical lithography and reactive ion beam etching. In a next step, the electrode edges and the surrounding film surface were covered by a 100 nm Y:ZrO_2 insulating layer deposited using pulsed laser deposition at room temperature. The repetition rate was 5 Hz and the spot size was 1.5 mm^2 at a target-to-substrate distance of 60 mm in an oxygen atmosphere of 10^{-4} mbar. The laser fluence was 2.1 J cm^{-2} (optical lithography and lift-off after pulsed laser deposition). This insulating layer allows for contacting the Pt electrode with Pt/Au leads (electron beam evaporation of an additional 10 nm layer of Pt followed by 130 nm of Au), which are separated from the continuous bottom electrode. The leads connect to the top electrode at one specific position (the region of interest described in the main text) and allow for an electrical connection far from the region of interest. This is important, as it was found that direct contact of the region of interest to the electrical probe could lead to melting of the specimen.

Thin specimens suitable for TEM analysis were prepared using an FEI Strata 400 focused ion beam milling tool. The specimens were thinned to 100 nm using first a 30 kV and then an 8 kV operating voltage, before cleaning either side of the specimen for 30 seconds using 2 kV ions. The specimens were then mounted in a Nanofactory biasing holder using conducting epoxy,

such that the substrate was connected electrically to the biasing chip. Before specimen preparation, the top of the specimen was protected with marker pen ink, which was removed by plasma cleaning just before the biasing experiments, such that the top Au contact was exposed for electrical probing. A piezo-controlled tungsten tip was landed onto the Au top contact. The key to these experiments was to position the electrical contact far from the region of interest to control the effects of Joule heating.

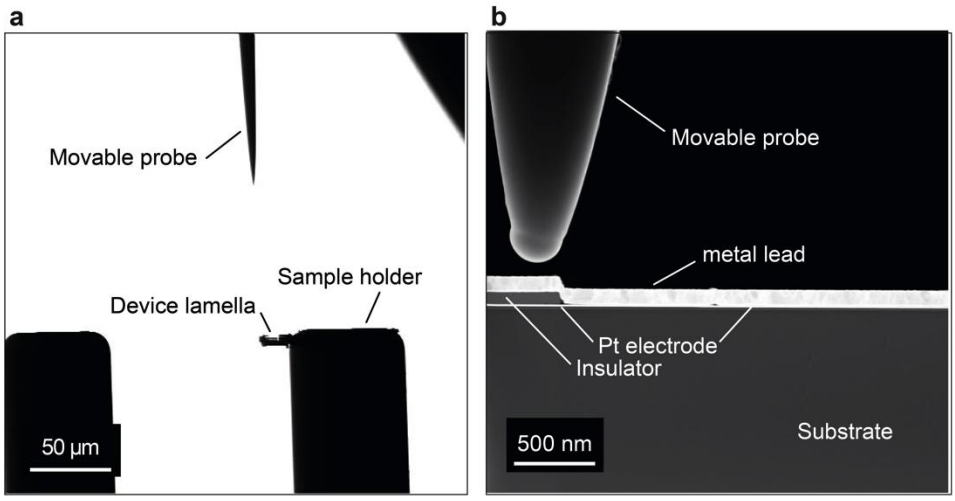

Figure S1. *In-situ* contacting. (a) The sample holder and the movable probe are shown with very low magnification. The memristive device is on the small lamella attached to the sample holder. (b) zoom-in to the device.

REVERSIBILITY OF THE VALENCE CHANGES DURING SWITCHING

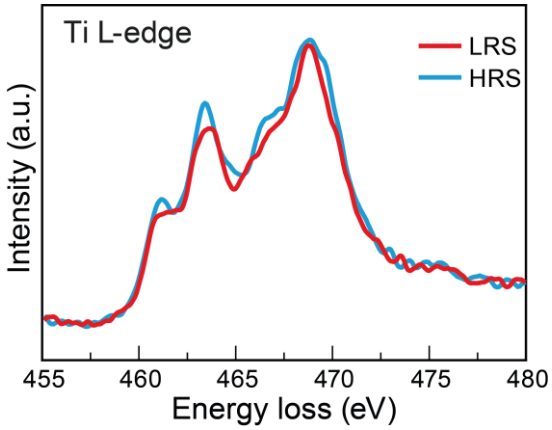

Figure S2. EEL spectra for the LRS and HRS from further switching experiments. The Ti L-edge spectra for the LRS and HRS verify that the Ti valence change is reversible during the *in situ* experiments.

HORIZONTAL EXTENT OF THE REDOX REACTION

A larger field of view was examined to determine the size and position of the redox-active region of the device. Supplementary Fig. 2a shows a large-scale HAADF STEM image of the previous region of interest. EELS maps were acquired across a several-µm-wide region to assess the changes in oxidation state. The region underneath the contact, between the metal lead and the top electrode labelled 'A', is the part of the device that is closest to the tungsten probe and where any switching-related changes were originally assumed to occur. Supplementary Fig. 2b shows Ti

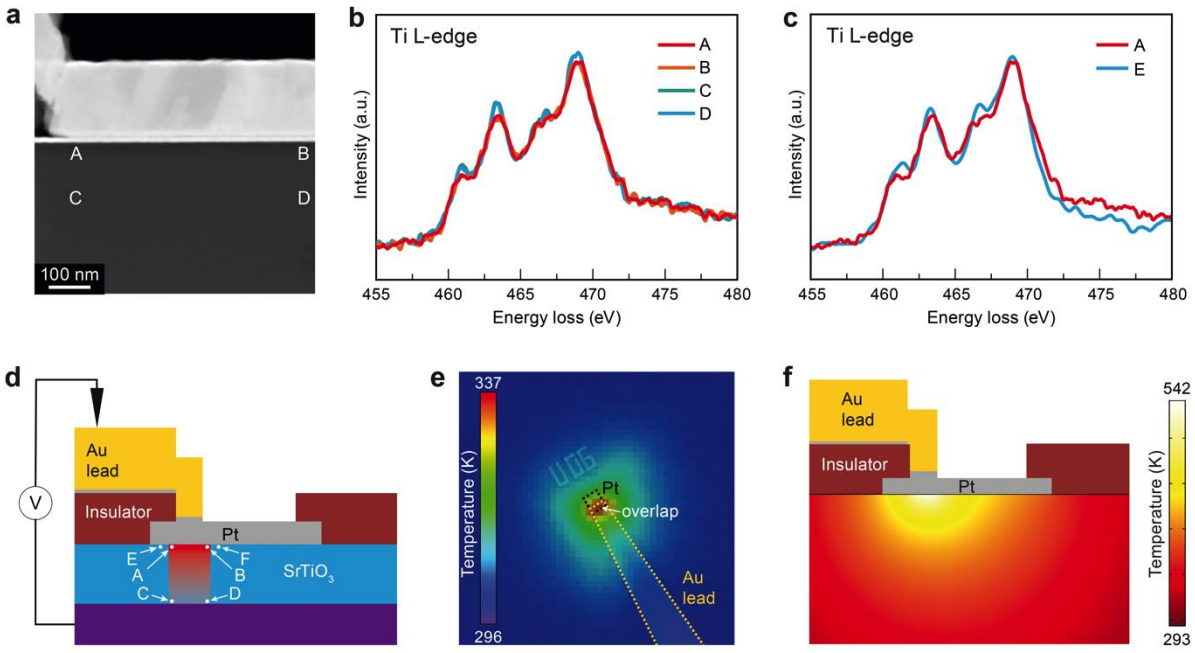

Figure S3. Horizontal extent of the redox reaction. (a) HAADF STEM image of the region of interest at low magnification. (b) Ti L-edge spectra acquired from the different regions indicated in (a). (c) Ti L-edge EEL spectra acquired from a representative region (point E, as indicated in (d)) outside the area visible in (a), compared with the spectrum from point A. At point E, there is no visible Ti^{3+} contribution. The same observation is true for point F (data not shown). (d) Schematic of the specimen, indicating the regions where changes occurred during the switching experiments. (e) Thermal image of a similar device overlaid with an optical micrograph during the Set process. The device has the same layer stack and metal lead as the TEM specimen. The top electrode area is indicated by a black dashed line. The metal lead is indicated by a yellow dashed line. The hottest temperatures are measured in the overlap area of the electrode and the metal lead. (f) Part of a 2D electro-thermal simulation. The simulated

temperature in the $SrTiO_3$ and Nb:$SrTiO_3$ layers is depicted according to a color code. The top layers are magnified with respect to their height, but not their width, to enable identification of the hot-spot. The highest temperature is reached beneath the part of the Pt top electrode that is capped with the Pt/Au lead.

L-edge spectra for the different regions indicated in Supplementary Fig. 2a. Here, it can be seen that the $SrTiO_3$ underwent a valence change from mainly Ti^{4+} to a mixture of Ti^{4+} and Ti^{3+} at point A and point B (and at each point between A and B), while points C and D at the bottom interface are only consistent with the presence of Ti^{4+}. $SrTiO_3$ regions further away from the contact area between the metal lead and the top electrode (but still underneath the metal electrode) do not exhibit any sign of a valence change (points E and F in Supplementary Figs 2c and d), as depicted schematically in Supplementary Fig. 2d. On the one hand, these observations show that the redox reaction has a rather large spatial extent of ~3 µm in the lateral direction, which corresponds well with previous observations[1]. On the other hand, it is clear that the redox reaction does not occur under the entire electrode area, but instead in a preferred position close to the metal lead. These observations are consistent with a spatially extended process, in which localization may be induced by the boundary conditions. The most obvious reason why the redox reaction could be located in a specific contact-area-defined region is the role of Joule heating, which is usually necessary to enable the valence change[2]. This hypothesis was verified using thermal imaging of a similar device during the Set process (Supplementary Fig. 2e), which clearly showed that a local hot-spot is located in the contact area between metal lead and the top electrode.

In order to clarify the origin of this hot-spot, an electro-thermal simulation was performed to solve the stationary current continuity equation and the heat equation for the electric potential and temperature in the entire specimen (Supplementary Fig. 2f). The current continuity equation and the heat equation need to be solved self-consistently with appropriate boundary conditions. Here, the numerical FEM software COMSOL Multiphysics was used. In its stationary form, the current continuity equation is

$$\nabla J = -\nabla(\sigma \nabla V) = 0 \qquad \text{(Supplementary Equation 1)}$$

where V is the potential, J is the current density and σ is the electrical conductivity. Considering Joule heating, the stationary heat equation

$$-\nabla(k \nabla T) = \frac{J^2}{\sigma} \qquad \text{(Supplementary Equation 2)}$$

is solved for temperature T with thermal conductivity k. The 2D electro-thermal model is sketched in Supplementary Fig. 3 for an out-of-plane thickness of 100 nm. Whereas Supplementary Fig. 3a is true to scale, the layers on top of the $SrTiO_3$, i.e. the Pt, Au and YSZ layers, are shown enlarged with respect to their height in Supplementary Fig. 3b.

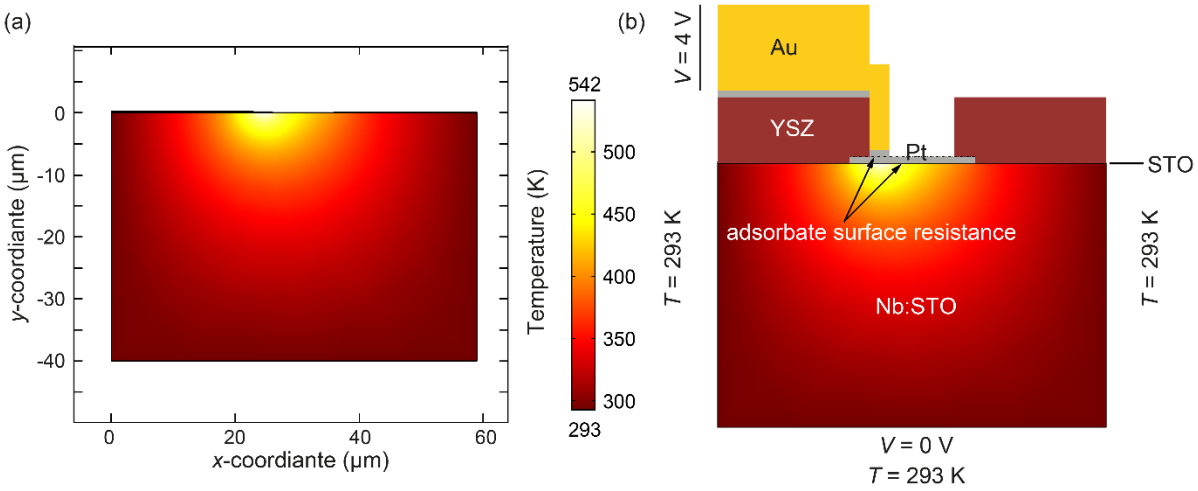

Figure S4. Electro-thermal simulation. (a) The device structure is shown true to scale. The results of the simulation for the temperature are depicted using a color code, with white signifying the highest temperature and dark red the lowest temperature, which is room temperature (293 K). As the top layers are too small to be identified, the same image is shown in (b) with the top layers enlarged. They are magnified with respect to their height but not their width. The highest temperature is reached beneath the part of the Pt top electrode that is capped with the Pt/Au lead.

As the Nb:$SrTiO_3$ bottom electrode has a thickness of 30 µm, the 20 nm $SrTiO_3$ layer is too thin to be identified. Besides the Au electrode's left boundary and the bottom electrode's lower boundary, which are set to a potential of 4 V and ground, respectively, all of the other outerboundaries are electrically insulating. In addition, the outer boundaries of the top layers to

air are defined as thermally insulating, as heat dissipation to air is negligible. The other outer boundaries are far from the hot-spot and are set to room temperature. A contact resistance above and underneath the Pt top electrode has to be considered. This is justified by the observation of a thin residue layer between the metal lead and the top electrode (the dark shadow in Supplementary Fig. 2a). As a result, a voltage divider is present between the oxide and the contact resistances and more heat is dissipated in the part of the top electrode that is in contact with the lead. In order to incorporate the influence of the adsorbate layers on top of the $SrTiO_3$ and between the Pt layers, a surface resistance with resistivity ρ_s is included in the model. All of the parameters are given in Supplementary Table 1. In order to identify the location of the highest temperature, the temperature in the $SrTiO_3$ layer 2 nm below the top electrode is plotted in Supplementary Fig. 4 as a function of the *x*-coordinate. The highest temperature is reached beneath the part of the Pt top electrode that is capped with Au. The location of the hottest spot is highly dependent on the electrical conductivity of $SrTiO_3$ and the adsorbate's surface resistivity, but the result is not limited to a unique parameter set. The result of the simulation is consistent with the experimentally verified local hot-spot and explains why the valence change is only observed in this preferred position.

Supplementary Table 1. Material parameters used in the electro-thermal simulation.

	σ (S/m)	k (W/(m·K))	$\rho_{\text{adsorbate}}$ ($\Omega \cdot m^2$)
Nb:$SrTiO_3$	$1 \cdot 10^6$	12	
$SrTiO_3$	0.7 or 0.3 (fitted)	12 [3]	
Pt	$1.66 \cdot 10^6$ (measured)	11.9 †	
Y:ZrO_2	$1 \cdot 10^{-6}$	2 [4]	
Au	$3.33 \cdot 10^6$ (measured)	26.4 †	
adsorbate layer			$1 \cdot 10^{-8}$ or $5 \cdot 10^{-9}$ (fitted)

† The Pt and Au electrical conductivities, which were measured in van der Pauw geometry on reference layers of the same thicknesses, are smaller than their literature values by a factor of 6 and 12, respectively. According to the Wiedemann-Franz law, the thermal conductivities are reduced by the same factor. The electrical conductivity of the $SrTiO_3$ layer and the adsorbate's surface resistivity are fitted to obtain 100 μA at 4 V.

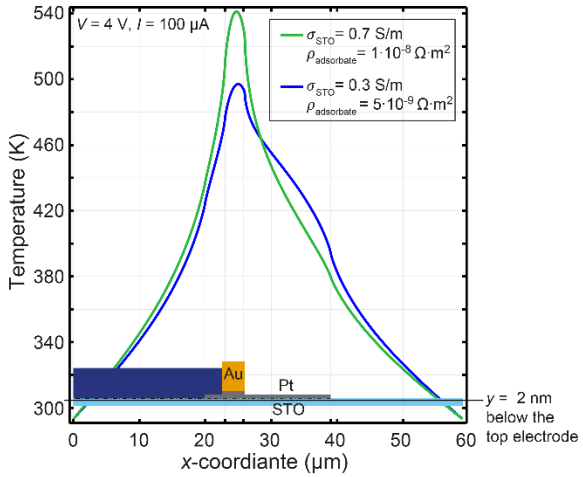

Figure S5. Influence of simulation parameters on the temperature profile. The temperature in the STO layer 2 nm below the top electrode is plotted as a function of the *x*-coordinate for two parameter sets of σ_{STO} and $\rho_{adsorbate}$. For both parameter sets, the current is 100 µA for an applied voltage of 4 V. The highest temperature is reached beneath the part of the Pt top electrode that is capped with the Pt/Au lead.

DRIFT-DIFFUSION MODEL

The *I-V* characteristics and the evolution of the oxygen vacancy profiles shown in Figs 3f and i of the main text were simulated using a 1D numerical model of coupled ionic-electronic transport in the oxide [5]. The simulations are based on a self-written program code employing the Pardiso solver from the Intel Math Kernel Library[6]. The model geometry consists of the oxide layer bounded by a high work-function electrode at $x = 0$ representing the Schottky-like Pt electrode and a low work-function electrode at $x = L$ representing the ohmic Nb:$SrTiO_3$ electrode. The oxide layer is assumed to be donor-doped by two-fold-ionizable oxygen vacancies of donor concentration $N_{VO}(x)$, as specified in Figs 4d and g. Further parameters used in the simulations are given in Supplementary Table 2. The underlying system of equations involves the Poisson equation

$$\nabla\left(\varepsilon_0\varepsilon_r\nabla\psi\right) = -e\left(n - N_{VO}^{+} - 2N_{VO}^{2+}\right), \qquad \text{(Supplementary Equation 3)}$$

which is solved self-consistently in an inner loop along with the steady-state drift-diffusion equation for electrons

$$\nabla\left(\mu_n n\nabla\psi - D_n\nabla n\right) = \pm\frac{\partial j_{n,\text{tunnel}}}{\partial x}. \qquad \text{(Supplementary Equation 4)}$$

In the above equations, ε_0 is the free space permittivity, ε_r is the relative permittivity of the oxide, ψ is the electrostatic potential, e is the elementary charge, n is the electron concentration, N_{VO}^{+} (N_{VO}^{2+}) is the concentration of the singly (doubly) ionized oxygen vacancies, μ_n is the electron mobility and D_n is the electron diffusion coefficient. The concentrations n, N_{VO}^{+} and N_{VO}^{2+} are obtained as outlined in ref. [7] using the effective density of states N_C (N_V) in the conduction (valence) band and the ionization energies $\Delta E_{VO}^{\times\to 1}$ and $\Delta E_{VO}^{1\to 2}$ for single and double ionization. The term on the right-hand side of Supplementary Equation 4 represents a local generation/recombination rate due to electron tunneling through the contact potential barrier, with the positive and negative sign of the tunneling current density $j_{n,\mathrm{tunnel}}$ corresponding to carrier creation behind and annihilation in front of the barrier, respectively. With the updated potential values, the evolution of the oxygen vacancy profile is computed for a certain time step by solving the time-dependent drift-diffusion equation for the doubly ionized species

$$\frac{\partial N_{VO}^{2+}}{\partial t} - \nabla\left(\mu_{VO} N_{VO}^{2+} \nabla\psi + D_{VO} \nabla N_{VO}^{2+}\right) = -R_{VO,2} \qquad \text{(Supplementary Equation 5)}$$

and the rate equations for the singly ionized and neutral species

$$\frac{\partial N_{VO}^{+}}{\partial t} = -R_{VO,1}, \qquad \text{(Supplementary Equation 6)}$$

$$\frac{\partial N_{VO}^{0}}{\partial t} = -R_{VO,0}. \qquad \text{(Supplementary Equation 7)}$$

Here, μ_{VO} is the donor mobility, D_{VO} the donor diffusion coefficient, N_{VO}^{0} the concentration of the neutral oxygen vacancies and $R_{VO,2}$, $R_{VO,1}$ and $R_{VO,0}$ the recombination rates that are derived from the laws of mass action for the ionization reactions along with the dopant ionization statistics [7]. The oxygen vacancy mobility and diffusion coefficient are assumed to be related to each other by the Einstein relation. They are assumed to be temperature activated, with the diffusion coefficient obeying the Arrhenius law

$$D_{VO} = D_0 \exp\left(-\frac{\Delta H_{D,VO}}{k_B T}\right)\left(1 - \frac{N_{VO}^{2+}}{N_{VO,max}}\right), \qquad \text{(Supplementary Equation 8)}$$

where k_B is the Boltzmann constant, T is the temperature, D_0 is the diffusion-coefficient prefactor, $\Delta H_{D,VO}$ is the migration enthalpy and $N_{VO,max}$ is the maximum possible oxygen vacancy concentration in the oxide layer. The temperature in the oxide layer is assumed to be uniform and is estimated by using the thermal resistance of the filament in 1D approximation according to

$$T = 300\ \mathrm{K} + \frac{L}{8k} j_{\mathrm{mean}} V_{\mathrm{a}}, \qquad \text{(Supplementary Equation 9)}$$

with k being an equivalent thermal conductivity of the 1D filament, j_{mean} the mean value of the current density (including electronic and ionic current contributions) and V_a the voltage drop across the oxide. The procedure of alternately solving an inner Gummel loop of Supplementary Equation 3 and Supplementary Equation 4 and calculating a time step by solving Supplementary Equation 5, Supplementary Equation 7 and Supplementary Equation 9 is repeated until the desired time is reached.

The boundary conditions for the Poisson equation are expressed in terms of the potential barrier heights at the contacts according to the expressions

$$\psi(0) = \psi_{\mathrm{i}}^0 + \frac{k_B T}{e}\eta_{\mathrm{Fn}}^0 - \phi_{\mathrm{Bn}}(0) + V_{\mathrm{a}}, \qquad \text{(Supplementary Equation 10)}$$

$$\psi(L) = \psi_{\mathrm{i}}^0 + \frac{k_B T}{e}\eta_{\mathrm{Fn}}^0 - \phi_{\mathrm{Bn}}(L). \qquad \text{(Supplementary Equation 11)}$$

Here, ψ_{i}^0 is the intrinsic potential in the undisturbed semiconductor, η_{Fn}^0 is the energy difference between the bottom of the conduction band and the Fermi level (normed by k_B/T) and ϕ_{Bn} is the effective potential barrier height. The latter term includes a barrier height modification $\Delta\phi_{Bn}$ due to image-force-induced barrier lowering (Schottky effect). It can be approximated using the nominal potential barrier height $\phi_{Bn0} = \phi_M - \chi_{SC,}$ where ϕ_M is the metal work function and χ_{SC} is the semiconductor electron affinity, and the electric field at the interface, yielding

$$\phi_{\mathrm{Bn}}(x) = \phi_{\mathrm{Bn0}}(x) \mp \Delta\phi_{\mathrm{Bn}}(x) \approx \phi_{\mathrm{Bn0}}(x) \mp \sqrt{\frac{e\left|\frac{d\psi(x)}{dx}\right|}{4\pi\varepsilon_0\varepsilon_{\mathrm{opt}}}} \qquad \text{(Supplementary Equation 12)}$$

with ε_{opt} being the high-frequency relative permittivity. In Supplementary Equation 12, the negative sign corresponds to a barrier reduction, which occurs in the case of a positive potential gradient at $x = 0$ or a negative potential gradient at $x = L$, while the positive sign corresponds to a

barrier enhancement, which occurs in the case of a negative potential gradient $x = 0$ or a positive potential gradient at $x = L$.

Electron transport across the metal-oxide boundary is modeled to occur via thermionic emission and tunneling. The electron current density at the boundary, which serves as the boundary condition for Supplementary Equation 4, is given by the thermionic-emission current density

$$j_{\mathrm{TE}}(0) = \frac{A^* T}{k_{\mathrm{B}}} \int_{E_{\mathrm{C}}(0)}^{\infty} N_{\mathrm{supply}}(E_x)\, dE_x, \qquad \text{(Supplementary Equation 13)}$$

$$j_{\mathrm{TE}}(L) = \frac{A^* T}{k_{\mathrm{B}}} \int_{E_{\mathrm{C}}(L)}^{\infty} N_{\mathrm{supply}}(E_x)\, dE_x, \qquad \text{(Supplementary Equation 14)}$$

where A^* is the effective Richardson constant, E_{C} is the conduction band energy and N_{supply} is the supply function. Similarly, the tunneling contribution, which is implemented as a local rate in the recombination term of Supplementary Equation 4, as outlined in [8], can be computed as

$$j_{\mathrm{tunnel}}(x) = \frac{A^* T}{k_{\mathrm{B}}} \int_{E_{\mathrm{C,min}}(x)}^{E_{\mathrm{C,max}}(x)} \mathcal{T}(E_x)\, N_{\mathrm{supply}}(E_x)\, dE_x. \qquad \text{(Supplementary Equation 13)}$$

Here, the integration is performed over the local energy difference of the control volume of the discretized domain. The transmission coefficient $\mathcal{T}(E_x)$ is calculated using the Wentzel-Kramers-Brillouin (WKB) approximation.

The electrodes are considered to be oxygen-blocking, implying zero current density j_{VO} across the electrode-oxide boundary. The boundary conditions for the oxygen-vacancy drift-diffusion equation thus read

$$j_{\mathrm{VO}}(0) = 0, \qquad \text{(Supplementary Equation 15)}$$

$$j_{\mathrm{VO}}(L) = 0. \qquad \text{(Supplementary Equation 16)}$$

Supplementary Table 2: Values of physical parameters used for the simulation of the *I-V* curves using the drift-diffusion model.

Symbol	Value	Symbol	Value
L	20 nm	$\Delta E_g(0\ \mathrm{K})$	3.3 eV
$R^{\dagger}$	10 nm	$\Delta E_{VO}^{\times\rightarrow 1}(0\ \mathrm{K})$	3 meV
N_C	$2.1\times10^{20}\ \mathrm{cm^{-3}}$	$\Delta E_{VO}^{1\rightarrow 2}(0\ \mathrm{K})$	30 meV
N_V	$1.3\times10^{20}\ \mathrm{cm^{-3}}$	$\beta_g^{\ddagger}$	$5.7\times10^{-4}\ \mathrm{eV\ K^{-1}}$
ε_r	10	$\phi_{Bn0}(0)$	0.7 V
$\varepsilon_{r,opt}$	5.5	$\phi_{Bn0}(L)$	0.05 V
D_0	$1.0\ \mathrm{cm^2/s}$	A^*	$120\ \mathrm{A\ cm^{-2}\ K^{-2}}$
ΔH_D	1.0 eV	$m_t^{\S}$	$9.1\times10^{-31}\ \mathrm{kg}$
$N_{VO,max}$	$5\times10^{22}\ \mathrm{cm^{-3}}$	$\tau_{VO}^{\times\rightarrow 1}$	1 ps
μ_n	$5.5\ \mathrm{cm^2(Vs)^{-1}}(T/300\ \mathrm{K})^{-2.23}$	$\tau_{VO}^{1\rightarrow 2}$	1 ps
		k	$1.25\ \mathrm{W(mK)^{-1}}$

† filament radius, used to obtain the current I

‡ temperature coefficient of the band gap

§ electron tunneling mass, needed to calculate the transmission coefficient

ATMOSPHERE-DEPENDENT RESISTIVE SWITCHING

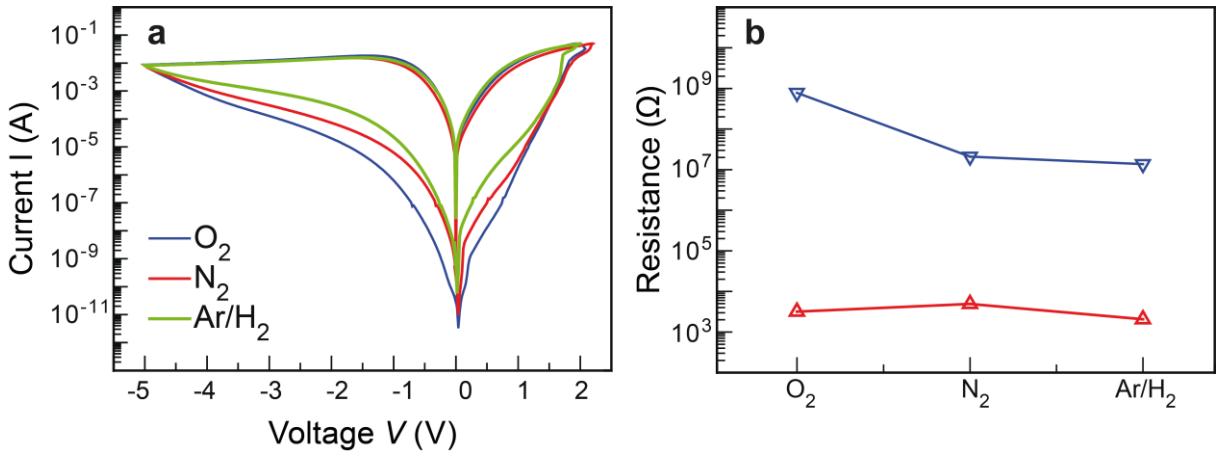

Figure S6. Atmosphere-dependent anomalous resistive switching of a typical µm-sized $SrTiO_3$ device exhibiting eightwise switching. The device was operated in an increasingly reducing atmosphere (O_2 followed by N_2 followed by an Ar/H_2 gas mixture (4 % H_2 in Ar)). Although it can be operated in each atmosphere, the Reset is deepest for oxidizing conditions, leading to a decrease in the HRS resistance with increasingly reducing atmosphere.

COEXISTANCE OF EIGHTWISE AND COUNTER-EIGHTWISE SWITCHING

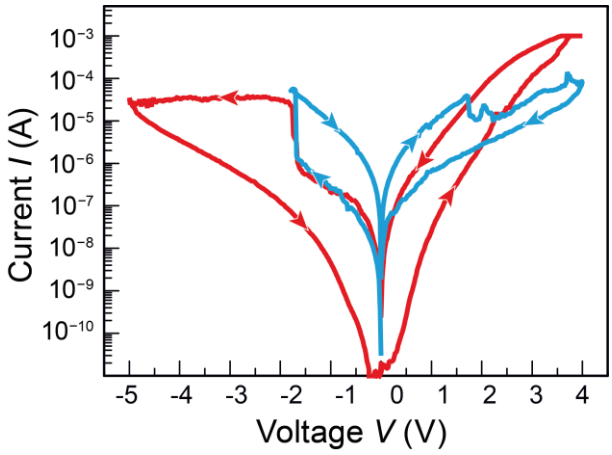

Figure S7. Coexistence of eightwise and counter-eightwise resistive switching in the same device. A 20 nm Fe:$SrTiO_3$ film with a 10x10 μm^2 Pt top electrode operated with a 1 mA current compliance. For low negative voltages, regular, counter-eightwise switching is obtained (blue curve). For high negative voltages, eightwise switching occurs (red curve).

SUPPORTING REFERENCES

[1] R. Muenstermann, T. Menke, R. Dittmann, R. Waser, *Adv. Mater.* **2010**, *22*, 4819.

[2] S. Menzel, M. Waters, A. Marchewka, U. Böttger, R. Dittmann, R. Waser, *Adv. Funct. Mater.* **2011**, *21*, 4487.

[3] Y. Suemune, *Journal of the Physical Society of Japan* **1965**, *20*, 174.

[4] K. Schlichting, N. Padture, P. Klemens, *J. Mater. Sci.* **2001**, *36*, 3003.

[5] A. Marchewka, R. Waser, S. Menzel, *2015 International Conference On Simulation of Semiconductor Processes and Devices (SISPAD), 9-11 September, Washington D.C, USA* **2015**, 297.

[6] Intel Math Kernel Library, http://software.intel.com/en-us/intel-mkl.

[7] A. Marchewka, B. Roesgen, K. Skaja, H. Du, C. L. Jia, J. Mayer, V. Rana, R. Waser, S. Menzel, *Adv. Electron. Mater.* **2016**, *2*, 1500233/1.

[8] M. Ieong, P. Solomon, S. Laux, H. Wong, D. Chidambarrao, *international electron devices meeting 1998 - technical digest* **1998**, 733.